

Re-entrant phase transitions and dynamics of a nanoconfined ionic liquid

Stefano Mossa*

Univ. Grenoble Alpes, CEA, CNRS, INAC-SYMMES, 38000 Grenoble, France

(Dated: May 17, 2022)

Ionic liquids constrained at interfaces or restricted in sub-nanometric pores are increasingly employed in modern technologies, including energy applications. Understanding the details of their behavior in these conditions is therefore crucial. By using Molecular Dynamics simulation we clarify the effect of confinement at the nanoscale on the static and dynamic properties of an ionic liquid. In particular, we focus on the interplay among the size of the ions, the planar pore width and the length scale associated to the long-range organization of polar and apolar domains present in the bulk material. By modulating both the temperature and the extent of the confinement we demonstrate the existence of a complex re-entrant phase behavior, including isotropic liquid and liquid-crystal-like phases with different symmetries. We describe in details the modifications of transport properties in the different phases, and discuss our findings in connection with recent experimental and theoretical work.

I. INTRODUCTION

In ionic liquids (ILs), molecular structures that frustrate the growth of the crystal phase at room conditions interfere with electrostatic interactions between ions and generate a behavior which is often at variance with that of molecular liquids and liquid crystals [1, 2]. On one side, this challenges in many ways our understanding of conventional electrolytes. On the other, it determines features which make ILs putative break-through materials for a few modern technologies, in particular for storage and conversion of energy [3–5]. In these applications ILs are often in contact with interfaces [1, 6], or confined in pores of sub-nanometric size [7], a situation that is highly non-trivial already for simple liquids [8]. A complete understanding of the physics of ILs in these configurations is therefore needed. Two examples, taken from recent experimental work on ILs confined at different length scales [9, 10], illustrate the scope of the challenge.

Nanoscale capillary freezing at room temperature has been demonstrated for an IL confined between a fixed substrate and the tip of a tuning fork Atomic Force Microscope, placed at a distance less than a well-defined threshold thickness [9]. This has been found to be as small as about 10 nm in the case of an insulating (mica) substrate, and to significantly increase with the metallic character of the latter. Although challenged by the work of [11], these results point to a dependence of the phase behavior of constrained ILs on the nature of the confining interfaces, which determines the critical pore size.

Other remarkable properties have been discovered in even thinner metallic pores. A X-Rays scattering and hybrid reverse Monte Carlo simulation study [10] has provided evidence of the existence of the so-called super-ionic state in ILs. This was predicted theoretically in [12–14], for pores widths comparable to the size of the adsorbed ions, in the sub-nanometric range. At these length

scales, the ionic properties of matter are modified by the occurrence of an exponential screening of the ion-ion electrostatic interactions, due to the image forces induced at the pore walls. These enable ions of the same sort to preferentially fill the pore, substantially modifying Coulombic ordering and causing an anomalous increase of the capacitive properties [15, 16], promising for supercapacitors technology.

These examples both ask for the comprehension of the role played by the size of the pore in determining the phase behavior of the adsorbed IL. Here we address this issue systematically by Molecular Dynamics simulation, focusing on structure and dynamics of an IL confined in nanometric slit pores. These range from sizes of a few Å to 5 nm, encompassing the entire interval from extreme confinement, with pore widths reduced to a fraction of the ion size, to situations where a bulk-like behavior is recovered. By also modifying the system temperature, we have sampled extensively the confined IL phase diagram. We present clear evidence that capillary crystallization is indeed possible for an IL confined at the nanoscale in an isolating pore. In addition, we demonstrate that the size of the (cat)ions, the width of the pore, and the length scale associated to the mesoscopic organization of ILs in the bulk [17], concur to determine a remarkable re-entrant phase behavior. This includes different ionic-liquid-crystal phases together with liquid states, which develop into a gel phase at high temperature and extreme confinement. Based on an extremely extended set of data, we characterize the structural properties of the different phases, and elucidate the features of their dynamics. Finally, we discuss our results with reference to recent experimental and theoretical work.

II. RESULTS: MODEL AND LENGTH SCALES

Recent computational studies of ILs have often employed quite spherical representations for the cation, including the restricted primitive model of [13], the popular model for $C_1\text{mim}$ (DMIM) of [18], or even the all-atoms

* stefano.mossa@cea.fr

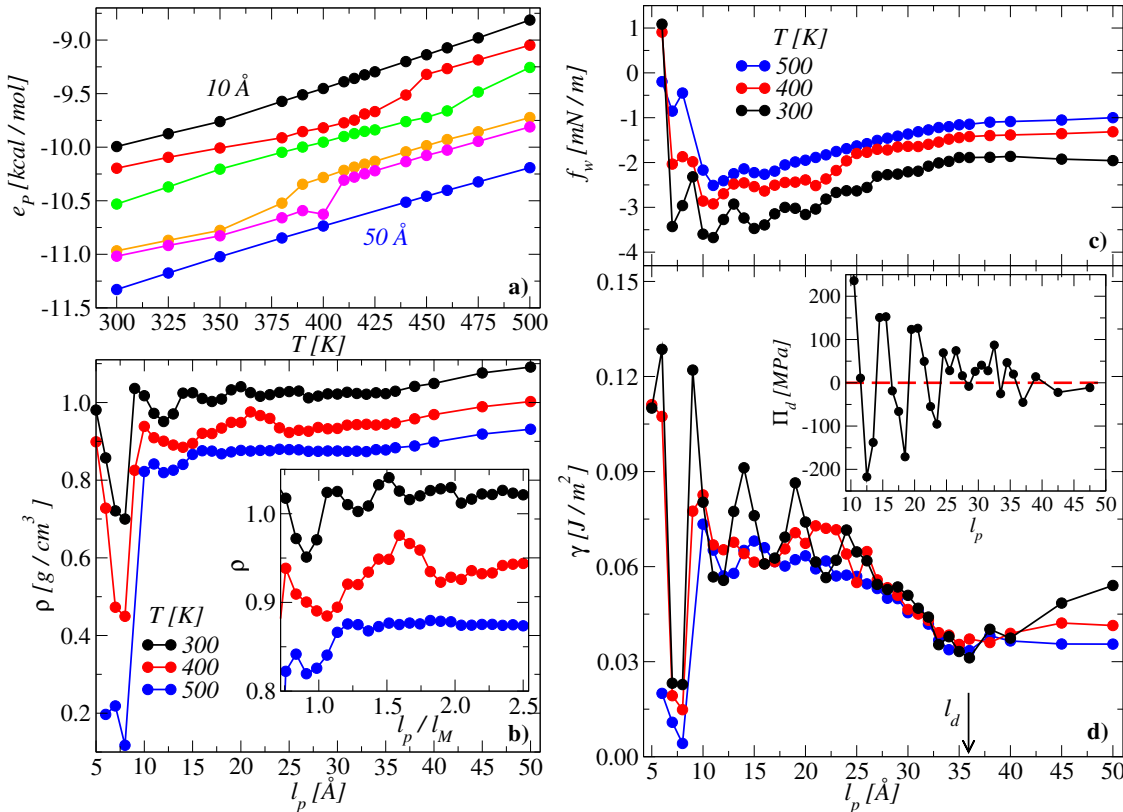


FIG. 1. T and l_p dependence of thermodynamic observables. a) Total per-bead potential energy, e_p , as a function of T , for $l_p = 10, 12, 14, 20, 22, 50 \text{ \AA}$, from top to bottom. We observe a discontinuous behavior of the data at intermediate values of l_p , which point to the crossing of T and l_p -dependent phase boundaries. b) l_p -dependence of the IL mass density ρ in the pore, at the indicated values of T . These data also show important discontinuities and point to substantial layering. In the inset we show the same data, now as a function of the pore width normalized to the length of the cation, l_p/l_M , to highlight the dependence on cation geometry at the different temperatures. c) l_p -dependence of f_w , the energy of interaction with the pore walls normalized to the total surface of the interfaces, at the indicated values of T . d) l_p -dependence of the surface tension, γ , at the same values of T . These data allow to be quantitative about the wetting properties of the adsorbed liquid phases. We also show l_d , indicated by the arrow. In the inset we show the disjoining pressure, Π_d , calculated from the data for $T = 300 \text{ K}$, as described in the text.

model for $C_1\text{mim}$ of [19]. At variance with these works, we consider the counter-ions couple $C_{10}\text{mim}^+\text{PF}_6^-$, with a strong molecular anisotropy. The anion, PF_6^- , is represented as a single interaction center without internal structure, to exacerbate the differences with the cation. The latter, in contrast, is now a rod-like molecule of length $l_M \simeq 13.2 \text{ \AA}$, described by an optimized version of the coarse-grained model of [20] (see Fig. 4).

This choice makes comfortable to highlight the interplay which involves l_M , the confining pore size l_p , and the length scale l_Q , associated to the mesoscopic nanostructuring of the bulk [17], which is particularly intense for ILs with long alkyl chains. (We can estimate $l_Q = 2\pi/Q^*$, where Q^* is the position of the low- Q prepeak appearing in the static structure factor, $S(Q)$, see below.) Indeed, when $l_p \gg l_Q$, the pore width does not interfere with the density fluctuations associated to the above feature. As a consequence, we can expect the confined system to behave similarly to the bulk. In the opposite limit, $l_p < l_M$, where the pore cannot accommodate a cation resting in the upward position, we should be able to probe extreme confinement conditions where

the cations lay almost parallel to the interface with the pore, and the system can practically be considered two-dimensional. In the intermediate range, finally, interesting features should appear as a consequence of the modifications induced by the pore on the adsorbed fluid density and orientational properties.

All the details of our re-parameterization of the force-field [20], molecular structures, implementation of the structureless slit pore (slab geometry in the $x-y$ plane), preparation of the adsorbed fluid, and clarifications on our numerical set-up (we work in the $(NP_{xy}T)$ -ensemble) in comparison with the thermodynamic conditions met in experiments, are deferred to the Sect. VII.

III. RESULTS: STATICS

A. Thermodynamics

We have considered an extremely large data set of phase points (see Methods section), and we describe in

details the data at temperatures $T = 300, 400,$ and 500 K. In Fig. 1 a) we plot the per-bead total potential energy $e_P = E_p/N$ of the IL beads as a function of T , at the indicated values of l_p . At $l_p = 50$ Å we find a behavior $\propto T^{3/5}$, typical of molecular liquids in the bulk [21]. Surprisingly, at lower values of l_p sudden drops appear at defined values of T , which depend on l_p and point to the crossing of some form of phase boundary. At the lowest shown value $l_p = 10$ Å in condition of extreme confinement, we recover a continuous dependence on T . A similarly discontinuous scenario is found by quantifying the modifications of the IL mass density in our constant- P_{xy} conditions. In Fig. 1 b), we show $\rho(l_p)$ at the indicated values of T . At large l_p , ρ decreases smoothly at all values of T . In the intermediate l_p -region, however, clear modulations develop, especially at the lower temperatures. In the inset we show the data comprised in this region, now as a function of l_p/l_M . This representation is useful to highlight that at $T = 400$ K the extrema points of ρ occur at $l_p/l_M \simeq 1, 3/2, 2$, therefore correlating to the formation in the pore of extremely ordered cations-rich layers, with a modulation which depends on the cation size. Note that, in conditions of extreme confinement, a deep drop in ρ appears at around $lz \simeq 7$ Å at all values of T , signaling the formation of a very low-density state. We will be more specific on this point below.

The observed modulations depend on the interaction of the IL with the pore walls. We have calculated f_w , the total interaction energy with the walls normalized to the pore surface (Fig. 1 c)). At large l_p , f_w assumes constant T -dependent values, until a T -independent cross-over at $l_d \simeq 5/2 l_M \simeq 35$ Å. For lower values of l_p , the curves follow the increase of the confinement in a non-trivial fashion, with modulations similar to those of ρ and wider at lower T . Note that f_w is the analogous of the force profiles measured by a Surface Force Apparatus [22], and shows a behavior very similar to that of many confined ILs, pointing to strong layering effects in the pore.

Important modifications also intervene in the wetting properties of the interfaces. We have calculated the surface tension as $\gamma(T, l_p) = l_p/2 \langle P_{zz} - 1/2(P_{xx} + P_{yy}) \rangle$, where the $P_{\alpha\beta}$ are the diagonal components of the pressure tensor. The data are shown in Fig. 1 d) as a function of l_p at the indicated T , and are intriguing. Indeed, at large l_p and low T they decrease smoothly, corresponding to the setup of a phase with wetting on the surface favored compared to the liquid, until a T -independent pore size corresponding to l_d . Next, γ undergoes an average T -independent increase by decreasing l_p with, however, the presence of modulations whose width is especially important at low- T and which follow those of f_w .

Also, γ is related to the total force exerted by the adsorbed fluid on the confining walls, the disjoining pressure [23], $\Pi_d(l_p) = -\partial_{l_p} \gamma(l_p)$, that we have calculated numerically and show in the inset for $T = 300$ K. $\Pi_d(l_p)$ features a damped oscillatory behavior [24], with a modulation dictated by the cation size. The oscillations are completely suppressed for $l_p \simeq l_d$, which can therefore be

interpreted as the pore size at which the pressure normal to the wall tends to that in the bulk (at the same temperature and chemical potential) [24], and determines the infinite-pore limit. Overall these data unambiguously point to important phase modifications of the adsorbed fluid following variations of both l_p and T .

B. Layering and orientational properties

The data presented above refer to observables averaged over the entire pore. They present, however, modifications that directly point to layering and therefore inhomogeneous space-dependent distributions of the different species in the pore, that are worth studying. We have precisely identified the positions of the cation/anion-rich domains in the different conditions by additionally coarse-graining the cation in terms of the centers of mass of the polar and apolar parts. We plot all our z -dependent (1-dim) data for all investigated values of l_p together in Fig. 2 a)-c) (for the polar head and the apolar tail of the cation and the anion, respectively) at $T = 400$ K in the form of a color map. Note that we have rescaled the x -axis as z/l_p in the range $[-0.5, 0.5]$, and the y -axis as l_p/l_M , to underline the correlation of the appearing features with the steric constraints associated to the rod-like cations. Also, the contrast has been enhanced rescaling the signal in the range $[0, 1]$ in all cases (see color code).

In conditions of extreme confinement, when the pore cannot accommodate a cation in the upright position, all species are unsurprisingly condensed in the center of the pore. In contrast, by increasing the pore width until $l_p \simeq l_M$ a clear partition occurs [25], with the apolar sections of the cations and the anions symmetrically localized at the interfaces, and the polar beads assuming a slightly more homogeneous structure shifted toward the center. (Note that, contrary to the case of larger pores, the cations maxima close to the interfaces originates from a single layer in an alternated head-to-toe conformation, as will be more clear from a visual inspection of the systems snapshots.) Interestingly, for $l_p > l_M$, the apolar tails coalesce at the interface, while the anions probability first condenses in the center of the pore and next partitions in two well-defined region symmetric to the pore axis. The polar heads of the cations follow a similar pattern.

This non-homogeneous distribution of the different moieties in the pore, induces strong space-dependent fluctuations in the mass distributions, that we plot in Fig. 2 d) and e) at $T = 400$ and 300 K, respectively. (All data are normalized in the $[0, 1]$ range.) Here, again, we find strong layering effects, particularly clear at $T = 300$ K, where a remarkable highly ordered three-layers structure is formed for $l_p/l_M \simeq 2$. This finding underlines again the importance of the steric constraints imposed by the elongated cations in fixing the periodicity of the modifications of the layered structure, while

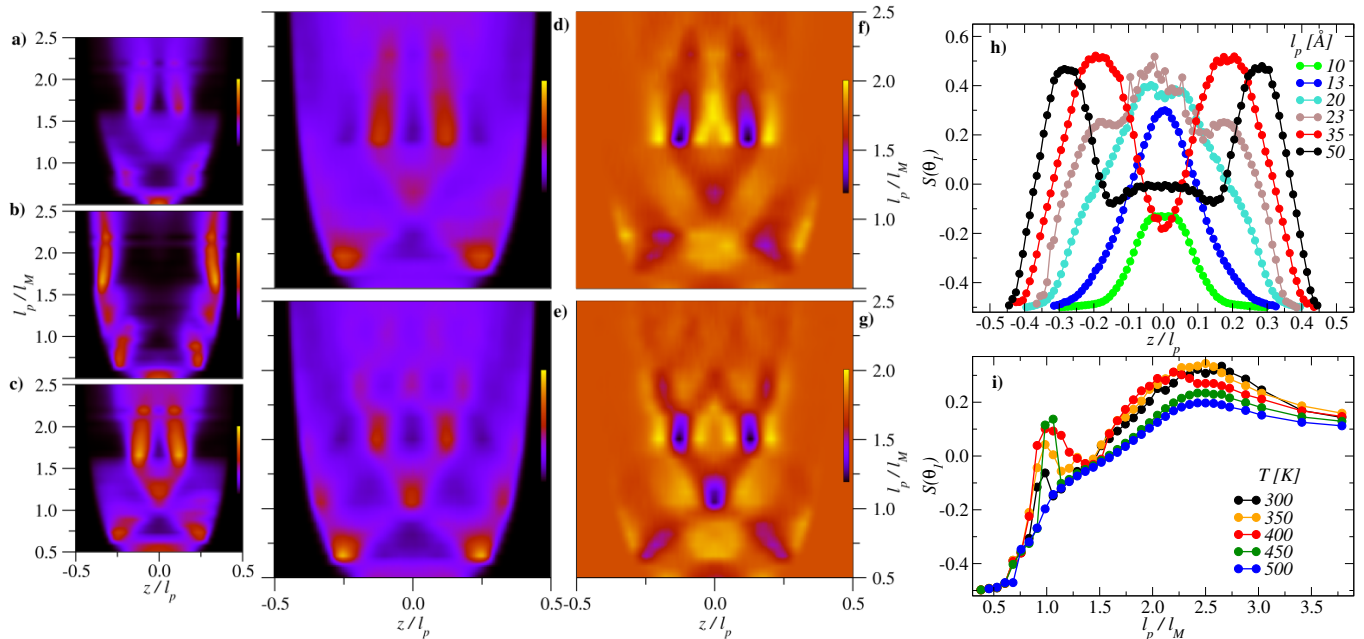


FIG. 2. Layering and orientational order. a)-c) Probability to find a bead associated to the polar and apolar parts of the cations and of the anions, respectively, at $T = 400$ K. The data are shown as a function of the position in the pore normalized to the pore size, z/l_p , for all values of l_p/l_M , and are renormalized in $[0, 1]$ (see color-box). d), e) Total mass distributions at $T = 400$ and 300 K, respectively, normalized in $[0, 1]$. f), g) Charge distributions at the same temperatures, normalized in the range $[-0.5, 0.5]$. h) z -dependence of the nematic order parameter $S(\theta_1)$ at $T = 400$ K at the indicated values of l_p . i) Average values of $S(\theta_1)$ as a function of l_p at the indicated values of T .

the actual distribution of mass and charge is primarily controlled by the anions. This last observation is corroborated by Fig. 2 f)-g), where we now plot the charge distribution, normalized in $[-0.5, 0.5]$. We note immediately that the black (most negative) spots perfectly match the maxima in the mass distributions, with a complete ordering of the adsorbed negative charge.

The above modifications are associated to space-dependent changes of the orientation of the cations. We have calculated the nematic order parameter, $S(\theta) = 1/2(3 \cos^2(\theta) - 1)$, where θ is the angle formed by a director associated to the cation molecule with the normal to the pore plane. We have chosen as the directors both the normalized dipole moment with respect to the cation center of mass (θ_1) and the normal to the plane identified by the three beads pertaining to the polar head (θ_2). We show the z -dependence of $S(\theta_1)$ in Fig. 2 h), for $T = 400$ K at the indicated values of l_p . The data at $l_p = 50$ Å indicate important alignment (orthogonal) of the cations adsorbed at the interfaces, with the formation of an extended bulk-like layer in the center of the pore, which disappears at 35 Å giving way to non-negligible alignment in the pore plane. Interestingly, the formation of a three-maxima (positive) structure is detected on lowering l_p , until the formation of a unique layer in the center of the pore strongly aligned in the plane in extreme confinement conditions, as expected.

The l_p -dependence of $S(\theta_1)$ integrated over the entire pore is shown in Fig. 2 i), at the indicated values of T . The overall behavior of the data is qualitatively T -

independent, except at the highest T . In extreme confinement conditions with $l_p \simeq 1/2 l_M$, we find $S(\theta_1) = -1/2$, as expected for a dipole constrained to rotate in the plane of the pore. Consistently $S(\theta_2) = 1$ (not shown), which corresponds to the imidazolium plane lying parallel to the pore walls. By increasing l_p , $S(\theta_1)$ first increases reaching a positive maximum at exactly $l_p = l_M$ and pointing to some form of (smectic) order, as it will be clear below. Next, it decreases following an increase of orientational disorder associated to mass reorganization. The subsequent increase reaches a maximum for $l_p \simeq 5/2 l_M$ corresponding to substantial nematic order, eventually tending to the isotropic value $S(\theta_1) \simeq 0$. Interestingly, while $S(\theta_1)$ couples to the macroscopic re-organization of the system, $S(\theta_2)$ probe more closely the variations of the local excluded volume, mirroring at all temperatures the modulations of the density (not shown).

C. The static structure factors

The data discussed above all point to a strong heterogeneity and non-trivial modifications of the structure of the adsorbed IL, following a temperature dependent interplay between the size of the rod-like cation and the width of the pore. We now focus on the correlations in space, which allow us to be more specific about the nature of the nanostructure of the system. We have calculated the (Neutrons-weighted) static structure factors directly at the microscopic level as $S(Q) \propto$

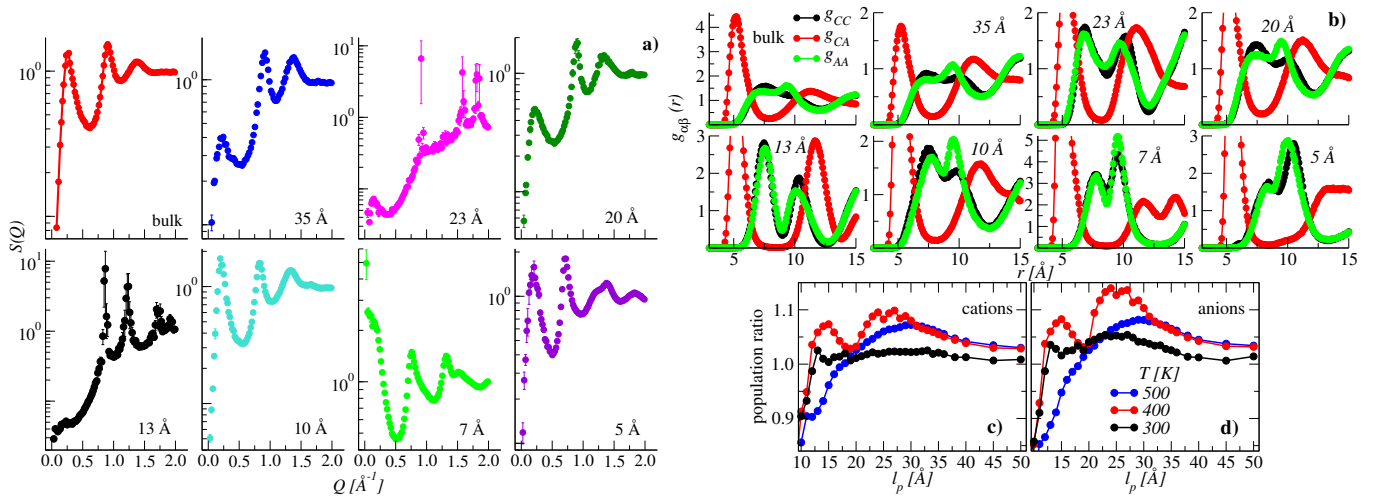


FIG. 3. Details of the static structure and coordination properties. a) Static structure factors, $S(Q)$, in the bulk and at the indicated values of l_p , at $T = 400$ K. Data are shown on logarithmic (y) scale. b) Partial pair distribution functions g_{CC} , g_{CA} , g_{AA} for the bulk and at the indicated values of l_p . c), d) l_p -dependence at the indicated temperatures of the fraction of co-ions in the first coordination shell normalized to the value in the bulk, for cations and anions respectively.

$1/N \langle \sum_{ij} b_\alpha b_\beta \exp[i\vec{Q} \cdot (r_i^\alpha - r_j^\beta)] \rangle$. Here, b_α is the coherent neutron scattering length for species α (see Table I), calculated for a united-atoms beads as the sum of the scattering lengths of its atomic components. $\langle \rangle$ indicates both the thermodynamic average and a spherical sampling over wave-vectors of modulus Q and polarized in the plane of the slab, $\vec{Q} = (Q_x, Q_y, 0)$.

Here we discuss in details the data at $T = 400$ K shown in Fig. 3 a), for the bulk and at the indicated values of l_p . In the bulk we find the $S(Q)$ typical of ionic liquids with bulky elongated cations [17], with the main diffraction peak at $\simeq 0.9 \text{ \AA}^{-1}$ and the remarkable pre-peak located at $Q^* \simeq 0.25 \text{ \AA}^{-1}$. This feature corresponds to a typical length scale $l_Q = 2\pi/Q^* \simeq 25 \text{ \AA} \simeq 2l_M$, which can be associated to a mesoscale structuration of the three-dimensional network of the polar domains [26]. The pre-peak is still present in mild confinement conditions corresponding to $l_p \simeq l_d$, which is too large to completely destroy the density fluctuations at Q^* , but is already able to strongly suppress its intensity.

Surprisingly, for $l_p = 23 \text{ \AA}$, the $S(Q)$ shows clear Bragg peaks superimposed to a disordered-like background, similar to that in the bulk and also including a relic of the pre-peak at Q^* . The Bragg peaks are produced by correlations of the charged species, and are located at values of $Q_1 \simeq 0.9$ and $Q_2 \simeq 3^{1/2}Q_1 \simeq 1.5 \text{ \AA}^{-1}$, pointing to an ordered phase with a string-like (or lamellar) symmetry. Strikingly, these structure is modified at lower l_p , where a pocket of liquid-like states is observed, before entering a new ordered region, with peaks now located at values of $Q_1 \simeq 0.85$ and $Q_2 \simeq 2^{1/2}Q_1 \simeq 1.2 \text{ \AA}^{-1}$, indicating a simple-cubic symmetry. When $l_p < l_M$, where the density of Fig. 1 b) shows a deep minimum, the $S(Q)$ diverges for $Q \rightarrow \infty$, pointing to gas-liquid coexistence. We will see in the following that an almost perfect network is formed in these conditions, similar to the case

of an ionic liquid gel phase. At the lowest studied value of l_p , we recover again a homogeneous liquid-like state where, however, the pre-peak is now almost as intense as the first diffraction peak, pointing to a substantially increased degree of order at long length scales, as expected in extreme confinement.

The above observations are confirmed by visual inspection of the systems snapshots in Fig. 4, where we also show the model for the IL as a reference for the color code used. Note that the size of the anions (red) beads has been substantially enhanced to emphasize the underlying order. The snapshots are shown both from the top of the confining surfaces and on a lateral view, for $l_p = 23 \text{ \AA}$ (a) and b)) and 13 \AA (c) and d)), respectively. The lamellar and cubic symmetries are very clear, with the lateral views emphasizing a substantial breaking of Coulombic ordering, as we will see in the next section. Ordering is even more clear on the bottom panels, where one can appreciate the formation of a gel-like network (e) and of a more homogeneous structure (f)) in conditions of extreme confinement.

We have calculated the $S(Q)$ at all state points, which present features very similar to those discussed for $T = 400$ K, but corresponding to different values of l_p . In particular, data at $T = 300$ K are similar to those discussed above at large values of l_p , with modified locations of the transitions between phases at lower l_p , and without any intercalated liquid state. In contrast, at $T = 500$ K, the system keeps a liquid-like structure at all confinement sizes.

D. The pair distribution functions

We now dig more into the relative organization of the ions. We have calculated the partial pair distribution

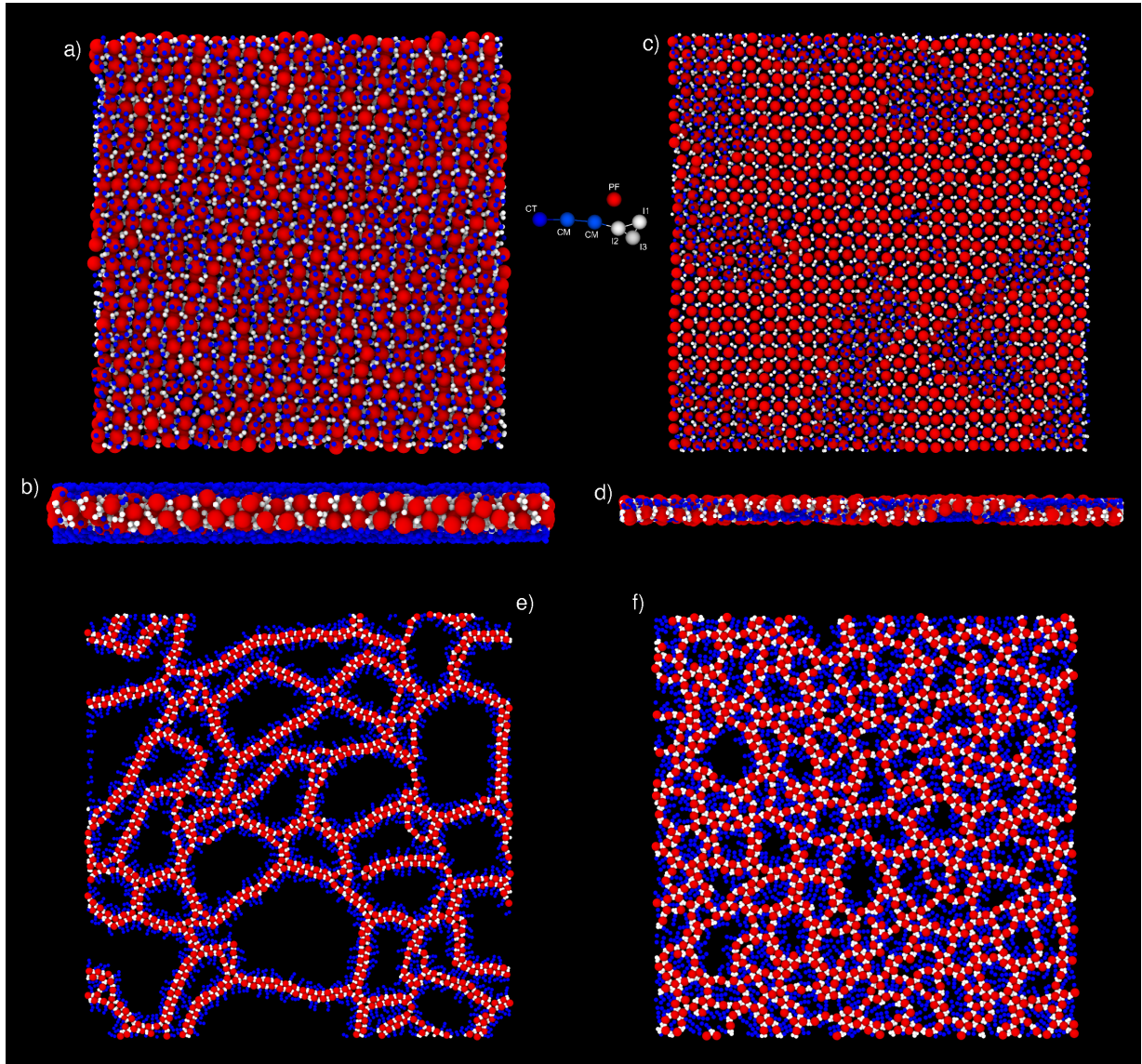


FIG. 4. Typical systems snapshots at chosen l_p . We show typical configurations of the system in different conditions of confinement, at $T = 400$ K. Colors are the same as in the IL model shown in the same figure, and beads nomenclature can be found in the Methods section. Note that we have exaggerated the size of anions beads, to underlying the symmetry of the ordered phases. a), b) Top and side view for $l_p = 23$ Å; c), d) Top and side view for $l_p = 13$ Å. In e) we show a typical gel-like configuration at $l_p = 7$ Å modifying into a more homogeneous configuration in extreme confinement conditions at $l_p = 5$ Å, shown in f).

functions $g_{\alpha\beta}$ with $\alpha, \beta = A, C$, considering the distances, r_{ij} , between the centers of mass of the polar head of the cations and the anions. Note that in our calculations we have considered the 3-dim r_{ij} and next have correctly normalized the data to take into account the slab geometry, recovering the usual limit $g(R \rightarrow \infty) \rightarrow 1$. Our data are shown in Fig. 3 b), for $T = 400$ K at the indicated values of l_p . The structure of g_{CA} shows no surprises, with an intense main peak centered at $\simeq 5$ Å in all cases, which points to the formation of ion pairs as customary in ILs [13]. g_{AA} and g_{CC} , in contrast, are more complex. In the bulk, g_{CC} shows a broad peak intercalated to the two main peaks of the g_{CA} . g_{AA} has

a very similar shape, except a tiny sub-peak developing at less than 10 Å which is more intense in mild confinement. At $l_p = 23$ Å the situation changes drastically, with a clear splitting of the above feature in two well-defined sub-peaks centered at $\simeq 7.5$ and 10 Å for both cases, with a more intense peak at shorter distances. A similar behavior reappears in a few of the following panels, mirroring the apparently erratic behavior of the $S(Q)$ discussed above.

We can be more quantitative on these observations by calculating directly the coordination number, i.e., counting the number of co-ions and counter-ions comprised in the first coordination shell of any ion. This is defined

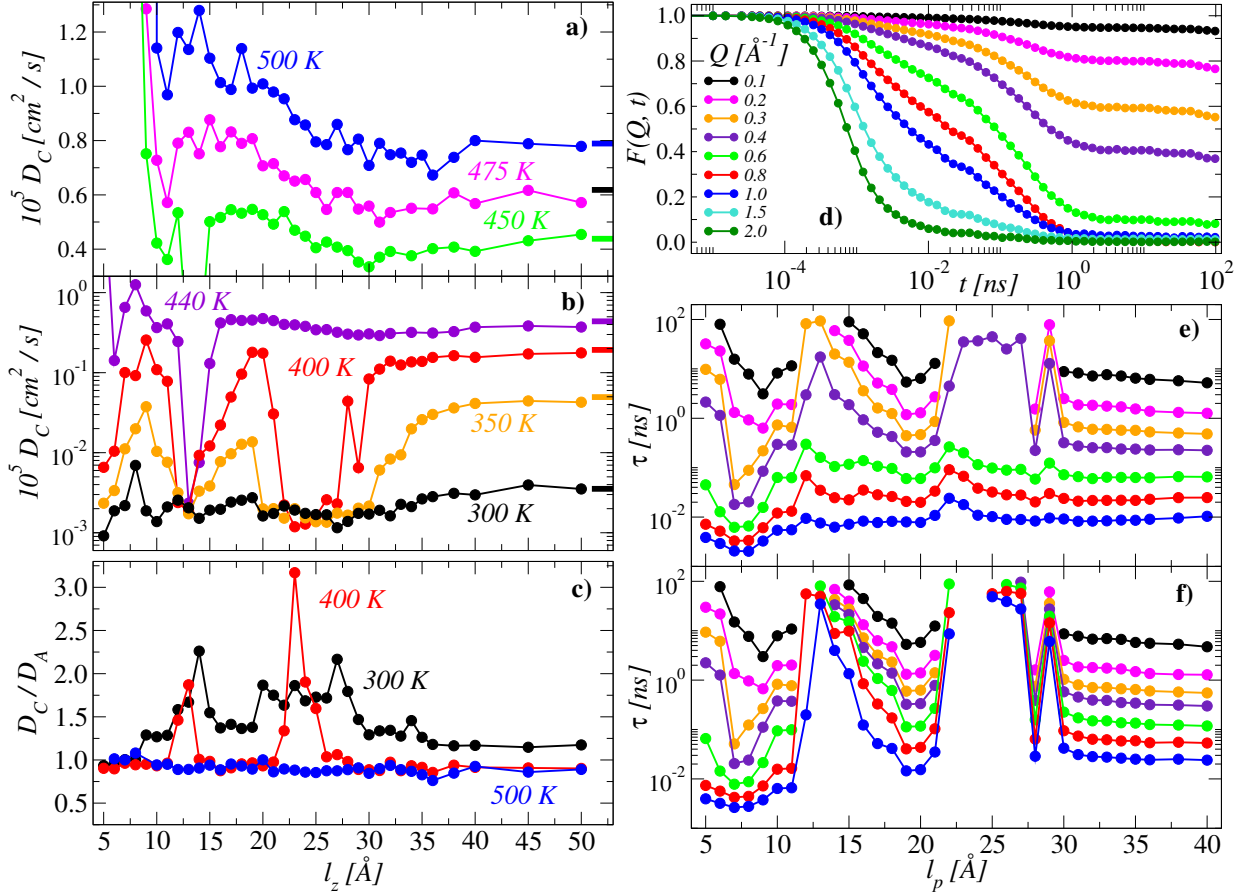


FIG. 5. Details of the dynamics. a) l_p -dependence of the diffusion coefficients of the cations centers of mass, D_C , at the indicated high temperature values. The corresponding values in the bulk are indicated by the solid thick lines on the right. b) Same as in a) at the indicated lower values of temperature. The deep discontinuities corresponding to phase boundaries crossing are discussed in the main text. c) The ratios D_C/D_A of the diffusion coefficients of the cations over those of the anions at the indicated temperatures. d) Intermediate scattering functions, $F_s(Q, t)$, at the indicated values of Q and $T = 400$ K. The data are calculated for the cations centers of mass. In e) and f) we plot the relaxation times, $\tau(Q)$ for cations and anions respectively, calculated from the relation $F(Q, \tau) = 1/e$. The colors identifying different values of Q are the same as in panel d). These data show that for particular values of l_p the dynamics of cations and anions decouples, the latter falling out-of-equilibrium on the time scale of our simulation, at all investigated values of Q .

as the (3-dim) sphere centered on an ion and of radius $r_c = 8 \text{ \AA}$, the position of the first deep minimum of the g_{CA} . From these data we can extract the fraction of co-ions over the total number of nearest-neighbors, $p_{C,A} = n_{C,A}/(n_C + n_A)$, for the cations and anions respectively, in analogy with [10]. In Fig. 3 c) and d) we show $p_{C,A}$ normalized to the respective values in the bulk (the population ratio), as a function of l_p at the indicated temperatures, which directly provides us with the relative variation of the Coulombic ordering compared to the unconstrained case.

At $T = 500$ K, p slightly increases by lowering l_p , always staying above the bulk value and eventually decreasing for strong confinement. Surprisingly, at $T = 400$ K the curve is strongly modulated, with clear maxima at defined values of l_p , and reaches values about $\simeq 15\%$ higher than in the bulk in the case of the anions. This effect vanishes at low temperature, where the value stays constant slightly above one, until a very high extent of the confinement, where it eventually decreases.

Typical systems configurations responsible for the maxima at $l_p = 23$ and 13 \AA are those shown in the side views of Fig. 4 b) and d). Note that these structures are very similar to the cartoons contained in [10], and our data point indeed to a facilitated approach in the first coordination shell of any ion of other ions of the same sort. This would imply important modifications of the Coulombic ordering present in the bulk, similar to the findings of [12, 13]. We will address this point more in depth in the discussion section.

IV. RESULTS: DYNAMICS

The analysis above points to strong discontinuous structural modifications of the system by changing both temperature and the size of the slit pore, compatible with plain phase changes in different confinement conditions. To complete the characterization of our system and provide an overall rationalization of the results, we now need

to go deeper and clarify the modifications due to confinement on the dynamical behavior of the ions. Here we only focus on mass transport, with a Nernst-Einstein point of view. Future work will be devoted to clarify the ionic properties of the system, which goes beyond the scope of this article.

A. The diffusion coefficients

We start our analysis from the diffusion coefficients of cations and anions, extracted from the mean-squared displacements, $\langle R_{C,A}^2(t) \rangle = 1/N_{C,A} \sum_{i=1, N_{C,A}} |\mathbf{R}_i(t) - \mathbf{R}_i(0)|^2$. Here $N_A = N_C$ is the number of cations and anions, and $\mathbf{R}_i(t)$ is the projection on the xy -plane of the position vector of the center of mass of molecule i at time t . Normally the diffusion coefficient could be extracted from these data via the usual Einstein relation restricted to the xy -plane. This relation, however, is only exact in the Fickian limit and is not appropriate in cases where, due to the confinement, strong sub-diffusivity could appear. We have, in contrast, estimated $D = 1/4 \partial_t \langle R^2(t) \rangle$, from the local slope of the mean-squared displacement at long times. D is therefore to be intended, more precisely, as an effective diffusion coefficient, characterizing the slow dynamics of the system on the time scale of our simulation, of about $10^{-1} \mu s$. Of course, at large l_p we must recover a value close to that in the bulk. The data for the cations are reported in Fig. 5 a) and b) at the indicated high and low temperatures, respectively. In all cases we indicate the corresponding values in the bulk as solid thick lines, for reference.

Behavior at high and low temperatures differs drastically. At high temperatures $T > 440$ K, at large values of l_p one recovers the value of the bulk, followed by a shallow minimum. At around $l_p \simeq l_d$, D starts to increase and assumes values higher than in the bulk, at all T . This effect is not surprising and has been already reported in other work in both experiments and simulation [19] for C_1mim , where it was rationalized in terms of a pure geometric effect. Note that in that paper the crossover to an increasing D starting from the high- l_p limit was also identified around l_d . At variance with our work, however, that limit was already higher than the value in the bulk for $l_p > l_d$. We note that this increase mirrors perfectly an analogous increase in the surface tension (Fig. 1 d)), which can be rationalized as follows. In confinement conditions where the system stays in a stable liquid state, following an increase in surface tension molecules will tend to stay away from the interfaces. They will therefore move toward the center of the pore, where the dynamics usually has a more pronounced bulk-like character, with the net effect of increasing the average D value.

At low temperatures $T \leq 440$ K, we observe a completely different behavior (Fig. 5 b)). Indeed, the values of D are always below the value assumed in bulk, with the appearance of deep minima, at confinement sizes compat-

ible with the discontinuities observed in the thermodynamical and structural properties. Note that the minima correspond to decreases of almost two orders of magnitude for both ions, providing an unambiguous evidence of the frozen character of the ordered phases described above.

The data for the anions follow a qualitatively similar behavior, but an additional observation is in order. We plot at each l_p and at the indicated temperatures the ratio D_C/D_A in Fig. 5 c). At the highest temperature, this ratio remains slightly higher than one, similar to the case of the bulk [7]. By lowering T , however, corresponding to the discontinuities in $D_{A,C}$, the ratio increases up to a factor of three at $T = 400$ K. From these data we conclude that although at the phase boundaries both species are dramatically slowed down, their dynamics decouple. In particular, the anions properly freeze at the lattice site and, as a consequence, the cations settle in the remaining available volume. They are still able, however, to undergo non-vanishing local structural rearrangements (including intra-molecular movements), sliding along the lattice planes identified by the anions ionic crystal. Note that, especially in the case $T = 400$ K, the maxima precisely correspond to those of Fig. 3 d), establishing a correlation between the dynamic decoupling and the partial breaking of the Coulombic ordering.

B. The intermediate scattering functions

This scenario can be confirmed by looking at the Q -vector dependence of the self-intermediate scattering function, $F_s(Q, t) = 1/N_{C,A} \sum_{i=1, N_{C,A}} \exp -i\mathbf{Q} \cdot [\mathbf{R}_i(t) - \mathbf{R}_i(0)]$. Here we consider, again, the molecular centers of mass position vectors, and Q -vectors which are polarized in the plane of the pore. A subset of our data is shown in Fig. 5 d), for the cations at the indicated values of Q and $T = 400$ K. The details of these curves are quite complex and a detailed analysis goes beyond the scope of the present work. We describe all data in a concise way in terms of a single structural relaxation time, $\tau(Q)$, defined from the usual relation $F(Q, \tau) = 1/e$, avoiding any fitting procedure. The data are shown in Fig. 5 e) and f), for the cations and anions respectively.

For large values of l_p , the relaxation is constant at all values of Q , and very close to the bulk case for both ions. On lowering l_p , however, the relaxation time for cations exceeds the maximum time scale probed in our simulations ($\tau > 0.1 \mu s$) at small values of Q entering our accessible time window for larger values of Q , well above the value corresponding to the long-range structuration in the bulk. This is in contrast with the case of the anions, where the relaxation exceeds our time window at all values of Q , pointing to completely frozen density fluctuations. A similar scenario appears again at lower values of l_p , where however, relaxation time scales are reduced at high- Q values. Note that the two frozen regions are

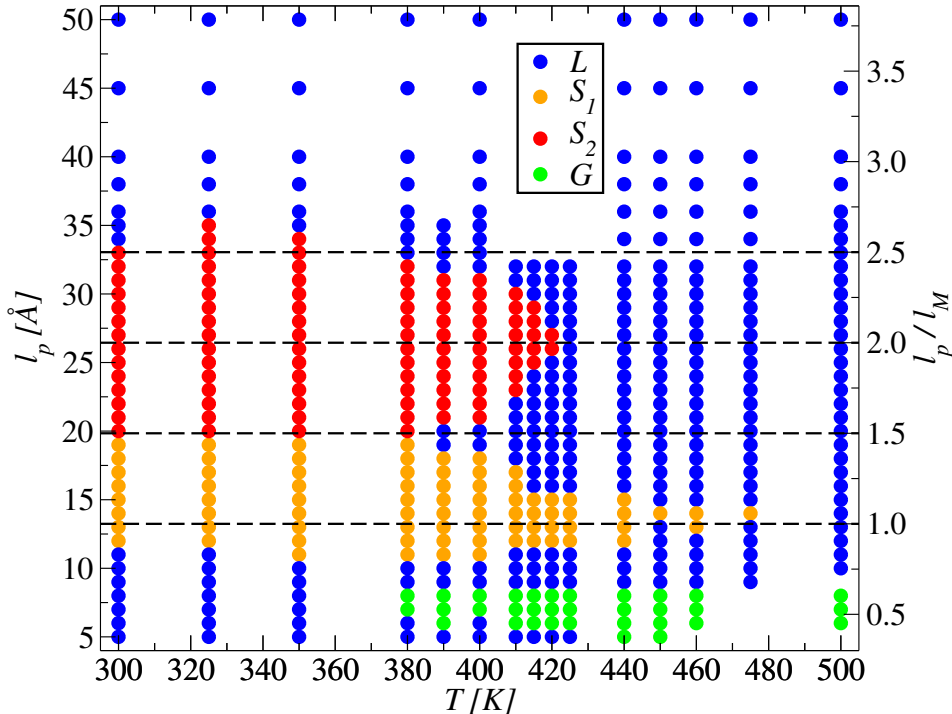


FIG. 6. Phase behavior of the confined IL. The $(T-l_p)$ phase diagram, on the basis of the discussed structural and dynamical properties. We also show the data in terms of l_p/l_M (right axis). This is the most important result of the present work, demonstrating the possibility of capillary freezing of an ionic liquid in a nanopore, the existence of multiple arrested states, and the occurrence of a re-entrant phase behavior with the stabilization of liquid-like pockets in situations of severe confinement. An interesting gel-like phase is also found, in conditions of very low density and high temperature, for confinement widths less than the rod-like cation molecular length.

separated by deep minima, corresponding to the intercalated liquid pockets, as expected. Eventually, in situation of extreme confinement, we find again a substantial decrease of the relaxation time associated to the formation of the gel and the almost 2-dim liquid described above.

V. RESULTS: THE $(T-l_p)$ PHASE DIAGRAM

Based on the thermodynamic data, static structure factors, direct visual inspection of system snapshots, and dynamical behavior, we distill all the information in the $(T-l_p)$ phase diagram of Fig. 6. We also show the data in terms of l_p/l_M (right axis), to help highlighting the interplay with the cation molecular length. In the high- l_p region for $l_p \geq l_d$ the confined ionic liquid is very similar to the bulk liquid at all temperatures (L), both regarding structure and dynamics, with the typical low- Q pre-peak in the $S(Q)$. Indeed, the extent of the confinement is still not sufficient to interfere destructively with the density fluctuations corresponding to this feature, the only visible effect being a decrease of its intensity.

The structure does not change much even at low- l_p and $T = 500$ K, where, however, a certain degree of cations nematic order sets in for $l_p < l_d$. Here we have demonstrated that the interaction force between the confining walls starts to be non negligible, with the typical oscillatory behavior of the disjoining pressure setting in. This

point also corresponds to an increase of the diffusion coefficients of both ions compared to the values in the bulk, which we have explained in terms of reinforced interaction of the adsorbed fluid with the pore walls. The situation does not change for lower temperatures, $T > 420$ K, where however, the system starts to cross the boundary of the phase S_1 at around $l_p/l_M \simeq 1$, eventually phase separating in extreme confinement, by entering the ionic liquid gel region (G).

For $T < 420$ K and $l_p < l_d$, the system starts to probe a remarkable re-entrant phase behavior, freezing in the two solid phases S_2 (lamellar order) and S_1 (cubic order). We have shown that the symmetry of the two solids is determined by the freezing of the (spherical) anions at the lattice sites, with the cations occupying the interstitials with substantial smectic order induced by the pore interfaces. Also, note that the two solid domains are centered around $l_p/l_M = 1$ and 2 , additionally highlighting the role played by the geometry of the cation in determining the position of the different boundaries in the phase diagram. We add, for completeness, that the boundaries separating S_1 and S_2 from the liquid apparently both have a discontinuous character, unlike to the finding of [27], for the case of confined water films.

The two solids are separated by an intercalated region of liquid water pockets, which stay stable for $T > 380$ K. At ($T = 380$ K and $l_p \simeq 20$ Å) we therefore find a solid-solid-liquid triple point, from which a solid-solid tran-

sition line originates which develops into the entire explored low-temperature region. Finally, for $l_p < 3/4 l_M$ a liquid region opens, which is stable at low temperatures but is destabilized in favor of an ionic liquid gel phase at higher temperatures.

VI. DISCUSSION

We discuss our results in relation with previous experimental and theoretical work. Some aspects of the structure/dynamics interplay we have described in this work can be generically identified in other systems. For instance, the re-entrant behavior in the phase diagram of Fig. 6 is similar to that demonstrated in [28], using density-functional theory for a model liquid crystal in a slit pore. A re-entrant melting transitions preventing solid-to-solid transformations and giving rise to intervening liquid phases has also been reported in [29] for the case of hard spheres in soft confinement. Finally, a re-entrant behavior of solid phases with intercalated water pockets has been discussed in the case of confined water nanofilms in [27]. In contrast with that paper, however, we find no sign of a continuous-like phase transition, with abrupt changes of the diffusion coefficients when crossing both boundaries following temperature changes. Features of the dynamics reminiscent of those described here have also been reported. As an example, on one side the effect of layering on the diffusion coefficient in the plane of the pore, with the alternation of maxima and minima, has been highlighted for the confined liquid films of [30]. On the other side, the non-monotonic dependence of the diffusion coefficient on the pore size has been reported for the confined hard spheres systems of [31], in the context of the glass transition phenomenon.

More specifically, it is instructive to discuss our results compared to two recent important pieces of work. First, nanoscale capillary freezing of ionic liquids confined between metallic interfaces has been demonstrated in [9], based on AFM measurements. Although the investigated IL (BmimBF₄) was different than that we have considered here, it is not baseless to speculate that the experiment probed the equivalent of the capillary freezing at $T = 300$ K from the liquid to the phase S_2 described above. A fact at odds with our findings, however, is that freezing was detected for confinement lengths substantially larger than $l_d \simeq 3.5$ nm, as it is the case here. This discrepancy could be due to differences in the experimental set-up compared to the simulation, as discussed in the Methods section. Also, note that in the same paper the crucial role played by the metallic character of the confining substrate was demonstrated, an ingredient which is absent in our calculations. These are however in agreement with the computer simulation used to backup the experimental data (see the supporting materials of [9]), which demonstrated a shift in the melting temperature controlled by the pore diameter by using insulating confining boundaries. We can conclude that the metallic

character of the pore seems to strongly enhance the occurrence of capillary freezing. This, however, is also possible in insulating pores but in more extreme confinement conditions. We close the discussion on this point by noticing that the findings of [9] are at odds with other measurements performed by means of a dynamic surface force apparatus [11], pointing to a possible observation length and time-scale dependence of the final result.

Second, confined ILs are of increasing interest in energy applications, including super-capacitors technology, due to peculiar capacity effects. These appear in conditions of strong confinement similar to that considered here, and are rationalized in terms of the insurgence of a superionic state [13]. The possible significance of our work for this issue is worth to be discussed. The formation of a superionic state has been predicted as a direct consequence of screening of the electrostatic interactions between ion pairs in extreme confinement in metallic pores. Very recently the existence of the of the superionic state has also been validated experimentally [10] in terms of significant breaking of the Coulombic ordering, based on diffraction data and reverse Monte Carlo methods. The similarity of the data of those papers with our results included in Fig. 3 c) and d), or with the system configurations of Fig. 4 b) and d) looks surprising if one recalls again that we have considered insulating boundaries. Here, the partial breaking of Coulombic ordering appears as the natural consequence of mass and charge distribution in the pore, controlled by the steric constraints associated to the cation molecular structure, and without any relation to charges induced at the boundaries.

We add that our simulations, for the first time at the best of our knowledge, also provide a complete coherent picture of both phase behavior and consequent dynamics changes of the adsorbed IL. In particular, we have shown that corresponding to the modifications of the charge distribution under confinement one can observe a remarkable decoupling of the dynamics of cations and anions. In our model these two features are therefore correlated, an other aspect shared with the superionic state [6]. Deeper insight, however, is needed to be conclusive on this point and attack other issues, as the modifications of ion conductivity beyond the Nernst-Einstein picture. We note, in conclusion, that our work highlights a possibly very different behavior of an IL adsorbed in nanometric pores of the same size, but at different temperatures. This poses a serious caveat on the legitimacy of extrapolating at room conditions properties observed at higher temperatures, a procedure very popular in simulation works.

VII. METHODS

A. The coarse-grained model for the IL

We have slightly re-parameterized the model of Ref. [20], which reproduces nicely the static properties of room temperature ionic liquids of the family 1-n-alkyl-3-

Bead type	m_α (g/mol)	q_α (e)	b_α
I1	35.5	0.356	6.23945
I2	34.5	0.292	9.98035
I3	26.0	0.152	5.815
CM	42.1	0.0	-2.5002
CT	43.1	0.0	-6.2411
PF	145.0	-0.8	39.054

TABLE I. Beads specifications including type, mass, charge and associated Neutrons scattering length, in the indicated units.

methylimidazolium hexafluorophosphate, but also shows a quite unrealistic dynamics, as noticed in Ref. [32]. More precisely, the self-diffusion coefficients of the cation are always smaller than those of the anion, a feature at odds with experiments. In real system, in fact, the cation diffuses faster than the anion. This is not expected on the basis of simple ionic size considerations [33], and can be attributed to the more dynamically heterogeneous environment of the cation with respect to the anion.

We have followed the simple methodology employed in [18] to improve over the parameterization of [34], by globally rescaling a few interaction parameters. The cation atoms are coarse-grained in beads, closely following [20]. As shown in Fig. 4, the imidazolium ring is composed of three charged beads, dubbed *I1*, *I2*, *I3*. The uncharged alkyl chain, whose length can be tuned to reproduce the entire C_n mim family, is formed in the present case (C_{10} mim) by two *CM* beads terminated by a *CT* unit. We have estimated the molecular length $l_M \simeq 13.2$ Å by measuring the distance of the two farthest beads d_{I1-CT} in the completely relaxed configuration of the isolated molecule. The anion is, in contrast, a simple point-like interaction center, *PF*. The values for the beads masses and charges, together with the Neutron scattering lengths used for the calculation of the static structure factor are reported in Tab. I.

The interaction potential is non-polarizable, a limitation common in these studies (see [35] for a rapid review of modeling of ionic liquids). The non-bonded interaction between two beads i and j of type α and β at distance $r_{ij}^{\alpha\beta} = r^{\alpha\beta}$ is the sum of a 9 – 6 Lennard Jones and a Coulomb term,

$$V(r^{\alpha\beta}) = \frac{27}{4}\epsilon^{\alpha\beta} \left[\left(\frac{\sigma^{\alpha\beta}}{r^{\alpha\beta}} \right)^9 - \left(\frac{\sigma^{\alpha\beta}}{r^{\alpha\beta}} \right)^6 \right] + \frac{1}{4\pi\epsilon_0} \frac{q^\alpha q^\beta}{r^{\alpha\beta}}. \quad (1)$$

The new values for the parameters are reported in Tab. II. All values of $\sigma^{\alpha\beta}$ have been rescaled by the same factor $f_\sigma = 0.948$ compared to those of [20]. The $\epsilon^{\alpha\beta}$ have been corrected in the same fashion, by a factor $f_\epsilon = 0.95$. In contrast, in order to cure the undesired features of the dynamics, we have substantially increased the strength of the *PF* – *PF* interactions, which now is $\epsilon^{PF-PF} \simeq 1.07$ kcal/mol. All other interaction energies

Beads pair	ϵ (kcal/mol)	σ (Å)
I1-I1	0.3569	3.8868
I1-I2	0.3424	3.8394
I1-I3	0.2603	3.8394
I1-CM	0.3309	4.0764
I1-CT	0.3718	4.1143
I1-PF	0.6178	4.8348
I2-I2	0.3284	3.8868
I2-I3	0.2497	3.8394
I2-CM	0.3174	4.0764
I2-CT	0.3566	4.1143
I2-PF	0.5926	4.8348
I3-I3	0.1898	3.4128
I3-CM	0.2413	3.5645
I3-CT	0.2711	3.6024
I3-PF	0.4505	4.5978
CM-CM	0.3990	4.2717
CM-CT	0.4218	4.3091
CM-PF	0.6532	4.6480
CT-CT	0.4455	4.3466
CT-PF	0.6903	4.6859
PF-PF	1.0694	4.9296

TABLE II. Force-field parameters used in the simulations. We have considered the values in [20], by doubling the value of ϵ^{PF-PF} with σ^{PF-PF} unchanged. Next we have globally rescaled all σ 's by $f_\sigma = 0.948$ and all ϵ 's by $f_\epsilon = 0.95$ and recalculated the interactions energy with *PF* by the usual mixing rule $(\epsilon_{\alpha\alpha}\epsilon_{\alpha\alpha})^{1/2}$.

involving the *PF*-bead have been generated by the usual mixing rule, $\epsilon^{\alpha\beta} = (\epsilon^{\alpha\alpha}\epsilon^{\beta\beta})^{1/2}$. Following these modifications, we did not need to tune the values of formal charges (see, for instance [18]), which are therefore the same as in [20]. In Eq. (1) the interactions are cut-off (but not shifted) at $r = r_C = 15$ Å, while the wave-vector part of the long-range Coulomb interactions in the slit pore (slab geometry) are calculated via the adapted method of [36], as we will see below. The values of the parameters for the harmonic bonds, $V_B(r) = k_B(r - r_o)^2$, and angles, $V_A(\theta) = k_A(\theta - \theta_o)^2$, are the same as in [20].

B. The confining pore

We consider a planar capillary (slit pore) with periodic boundary conditions in the $x - y$ plane. Confinement in a slab oriented with the normal in the \hat{z} -direction and width l_p is implemented by bounding the simulation domain with two continuous unstructured flat walls located at $l_w = \pm l_p/2$. Each wall interacts with a bead at $z_i = z$ by generating a force in the \hat{z} -direction, corresponding to

a potential [19],

$$V_w(z) = \epsilon_w \left[\frac{2}{15} \left(\frac{\sigma_w}{z} \right)^9 - \left(\frac{\sigma_w}{z} \right)^3 \right] \theta(z - z_w). \quad (2)$$

We have chosen $\epsilon_w = 0.2$ kcal/mol, $\sigma_w = 3$ Å, and $z_w = 2.5 \sigma_w = 7.5$ Å. Therefore, for $l_p < 2z_w = 15$ Å the beads interact with both walls. Obviously, we are aware of the fact that avoiding to consider a more realistic confinement, for instance by a crystalline lattices formed by immobile charged atoms, imposes limitations on our analysis (we cannot study capacitive features, for instance).

Care must be taken for the calculation of the interaction with the charge images in the non-periodic \hat{z} -direction. This is done by treating the system as if it was periodic in \hat{z} , but inserting empty volume between atom slabs and removing dipole inter-slab interactions so that slab-slab interactions are effectively turned off. The methodology behind the algorithm used is explained in [36]. Note that this procedure corresponds to an insulating pore configuration.

C. Simulation details

All calculations have been performed with LAMMPS [37]. The trajectories have been propagated in the $(NP_{xy}T)$ ensemble, where $L_z = l_p$ is fixed while $L_x = L_y$ are allowed to fluctuate to match the value $P_{xy} = 1$ atm. We have generated extremely extended data sets encompassing 15 values of temperatures in the range 300 to 500 K, and confinement lengths in the range 5 to 50 Å, for a total of 488 independent state points. In all cases the total number of interacting beads is $N = 7000$.

Initial systems configurations were prepared as follows. We started from a completely random configuration the system at $T = 500$ K in a simulation box extremely elongated in the non-periodic walls-bounded \hat{z} -direction, determining approximate Coulomb interactions truncated and screened according to the modified Wolf version of the damped shifted force model [38], with a damping parameter $\alpha = 0$. Next, we generated all pores with different widths by rapidly rescaling l_p to the desired values of l_p . We have checked that all initial configurations did not present any form of order. Each system

was subsequently allowed to evolve, thermalizing on time scales of the order of 10^2 ns at the lowest temperatures, followed by production runs of 10^2 ns for all states. The total simulation time exceeds the 2×10^2 ns in most cases. With this procedure and having avoided, in particular, to prepare initial configurations by compressing/dilating or cooling systems generated in different conditions, we are confident we have minimized possible correlations among pores. Finally, at each investigated value of T we have studied the corresponding system in the bulk, with the same number of ion pairs, values of the parameters involved in the simulation algorithms and on the same time scales. We can therefore count in all cases on the exact reference bulk configurations. More details on the bulk systems will be discussed in forthcoming publications.

We conclude with an observation on our simulations set-up compared to the typical thermodynamic conditions met in experiments. Here we have worked in thermodynamic conditions $P_{xx} = P_{yy} = 0$ which are not those found in experiments, where, in contrast, the chemical potential, μ , is held constant. The typical setup corresponds indeed to the triple point conditions where the pore is in contact with a liquid phase region surrounded by its vapour, these two buffer phases keeping μ constant in the pore, a procedure which is also possible in simulations [24], but is computationally more demanding than that we have employed here. At this point, every state we have investigated is in principle at a different value of μ , making arduous to propose a simple mapping to realistic thermodynamic conditions for an experiment pointing to demonstrate the re-entrant behavior, for instance. We note, however, that in Ref. [39] it was demonstrated that solvation forces, which play a crucial role in these system, are not very sensitive to changes in the chemical potential of the adsorbed fluid. This is reassuring in view of the relevance of our simulation for realistic experimental conditions.

ACKNOWLEDGMENTS

We are indebted to Benoit Coasne for a few enlightening discussions. We acknowledge support from the CEA funding program "DSM Energie".

-
- [1] Robert Hayes, Gregory G Warr, and Rob Atkin, "Structure and nanostructure in ionic liquids," *Chemical reviews* **115**, 6357–6426 (2015).
 - [2] Karel Goossens, Kathleen Lava, Christopher W Bielawski, and Koen Binnemans, "Ionic liquid crystals: versatile materials," *Chemical reviews* **116**, 4643–4807 (2016).
 - [3] Douglas R MacFarlane, Maria Forsyth, Patrick C

- Howlett, Mega Kar, Stefano Passerini, Jennifer M Pringle, Hiroyuki Ohno, Masayoshi Watanabe, Feng Yan, Wenjun Zheng, *et al.*, "Ionic liquids and their solid-state analogues as materials for energy generation and storage," *Nature Reviews Materials* **1**, 15005 (2016).
- [4] Masayoshi Watanabe, Morgan L Thomas, Shiguo Zhang, Kazuhide Ueno, Tomohiro Yasuda, and Kaoru Dokko, "Application of ionic liquids to energy storage and con-

- version materials and devices,” *Chemical reviews* (2017).
- [5] Patricia C Marr and Andrew C Marr, “Ionic liquid gel materials: applications in green and sustainable chemistry,” *Green Chemistry* **18**, 105–128 (2016).
 - [6] Maxim V Fedorov and Alexei A Kornyshev, “Ionic liquids at electrified interfaces,” *Chemical reviews* **114**, 2978–3036 (2014).
 - [7] Shiguo Zhang, Jiaheng Zhang, Yan Zhang, and Youquan Deng, “Nanoconfined ionic liquids,” *Chemical reviews* **117**, 6755–6833 (2016).
 - [8] C Alba-Simionesco, Benoit Coasne, G Dosseh, G Dudziak, KE Gubbins, R Radhakrishnan, and MJPCM Sliwinski-Bartkowiak, “Effects of confinement on freezing and melting,” *Journal of Physics: Condensed Matter* **18**, R15 (2006).
 - [9] Jean Comtet, Antoine Niguès, Vojtech Kaiser, Benoit Coasne, Lydéric Bocquet, and Alessandro Siria, “Nanoscale capillary freezing of ionic liquids confined between metallic interfaces and the role of electronic screening,” *Nature Materials* **16**, 634–639 (2017).
 - [10] Ryusuke Futamura, Taku Iiyama, Yuma Takasaki, Yury Gogotsi, Mark J Biggs, Mathieu Salanne, Julie Ségalini, Patrice Simon, and Katsumi Kaneko, “Partial breaking of the coulombic ordering of ionic liquids confined in carbon nanopores,” *Nature materials* **16**, 1225 (2017).
 - [11] Léo Garcia, Léa Jacquot, Elisabeth Charlaix, and Benjamin Cross, “Nano-mechanics of ionic liquids at dielectric and metallic interfaces,” *Faraday discussions* **206**, 443–457 (2018).
 - [12] S Kondrat and A Kornyshev, “Superionic state in double-layer capacitors with nanoporous electrodes,” *Journal of Physics: Condensed Matter* **23**, 022201 (2011).
 - [13] S Kondrat, Nikolaj Georgi, Maxim V Fedorov, and Alexei A Kornyshev, “A superionic state in nano-porous double-layer capacitors: insights from monte carlo simulations,” *Physical Chemistry Chemical Physics* **13**, 11359–11366 (2011).
 - [14] Maxym Dudka, Svyatoslav Kondrat, Alexei Kornyshev, and Gleb Oshanin, “Phase behaviour and structure of a superionic liquid in nonpolarized nanoconfinement,” *Journal of Physics: Condensed Matter* **28**, 464007 (2016).
 - [15] John Chmiola, G Yushin, Yury Gogotsi, Christele Portet, Patrice Simon, and Pierre-Louis Taberna, “Anomalous increase in carbon capacitance at pore sizes less than 1 nanometer,” *Science* **313**, 1760–1763 (2006).
 - [16] Céline Merlet, Benjamin Rotenberg, Paul A Madden, Pierre-Louis Taberna, Patrice Simon, Yury Gogotsi, and Mathieu Salanne, “On the molecular origin of supercapacitance in nanoporous carbon electrodes,” *Nature materials* **11**, 306 (2012).
 - [17] Alessandro Triolo, Olga Russina, Hans-Jurgen Bleif, and Emanuela Di Cola, “Nanoscale segregation in room temperature ionic liquids,” *The Journal of Physical Chemistry B* **111**, 4641–4644 (2007).
 - [18] Durba Roy and Mark Maroncelli, “An improved four-site ionic liquid model,” *The Journal of Physical Chemistry B* **114**, 12629–12631 (2010).
 - [19] Carlos Pinilla, Mario G Del Pópolo, Ruth M Lynden-Bell, and Jorge Kohanoff, “Structure and dynamics of a confined ionic liquid. topics of relevance to dye-sensitized solar cells,” *The Journal of Physical Chemistry B* **109**, 17922–17927 (2005).
 - [20] B Lokogowda Bhargava, Russell Devane, Michael L Klein, and Sundaram Balasubramanian, “Nanoscale organization in room temperature ionic liquids: a coarse grained molecular dynamics simulation study,” *Soft Matter* **3**, 1395–1400 (2007).
 - [21] Yaakov Rosenfeld and Pedro Tarazona, “Density functional theory and the asymptotic high density expansion of the free energy of classical solids and fluids,” *Molecular Physics* **95**, 141–150 (1998).
 - [22] Susan Perkin, Tim Albrecht, and Jacob Klein, “Layering and shear properties of an ionic liquid, 1-ethyl-3-methylimidazolium ethylsulfate, confined to nano-films between mica surfaces,” *Physical chemistry chemical physics* **12**, 1243–1247 (2010).
 - [23] Pierre-Gilles de Gennes, Françoise Brochard-Wyart, and David Quere, “Capillarity and wetting phenomena: Drops,” *Bubbles, Pearls, Waves* **336** (2004).
 - [24] Luis G Cámara and Fernando Bresme, “Molecular dynamics simulations of crystallization under confinement at triple point conditions,” *The Journal of chemical physics* **119**, 2792–2800 (2003).
 - [25] Alexander M Smith, Kevin RJ Lovelock, Nitya Nand Gosvami, Peter Licence, Andrew Dolan, Tom Welton, and Susan Perkin, “Monolayer to bilayer structural transition in confined pyrrolidinium-based ionic liquids,” *The journal of physical chemistry letters* **4**, 378–382 (2013).
 - [26] Juan C Araque, Jeevapani J Hettige, and Claudio J Margulis, “Modern room temperature ionic liquids, a simple guide to understanding their structure and how it may relate to dynamics,” *The Journal of Physical Chemistry B* **119**, 12727–12740 (2015).
 - [27] SungHo Han, MY Choi, Pradeep Kumar, and H Eugene Stanley, “Phase transitions in confined water nanofilms,” *Nature Physics* **6**, 685–689 (2010).
 - [28] D de Las Heras, E Velasco, and L Mederos, “Capillary smectization and layering in a confined liquid crystal,” *Physical review letters* **94**, 017801 (2005).
 - [29] Tine Curk, Anouk de Hoogh, Francisco J Martinez-Veracoechea, Erika Eiser, Daan Frenkel, Jure Dobnikar, and Mirjam E Leunissen, “Layering, freezing, and reentrant melting of hard spheres in soft confinement,” *Physical Review E* **85**, 021502 (2012).
 - [30] Jianping Gao, WD Luedtke, and Uzi Landman, “Layering transitions and dynamics of confined liquid films,” *Physical review letters* **79**, 705 (1997).
 - [31] Suvendu Mandal, Simon Lang, Markus Gross, Martin Oettel, Dierk Raabe, Thomas Franosch, and Fathollah Varnik, “Multiple reentrant glass transitions in confined hard-sphere glasses,” *Nature communications* **5**, 4435 (2014).
 - [32] Hossein Ali Karimi-Varzaneh, Florian Müller-Plathe, Sundaram Balasubramanian, and Paola Carbone, “Studying long-time dynamics of imidazolium-based ionic liquids with a systematically coarse-grained model,” *Physical Chemistry Chemical Physics* **12**, 4714–4724 (2010).
 - [33] Anna Martinelli, M Maréchal, Å Östlund, and J Cambedouzou, “Insights into the interplay between molecular structure and diffusional motion in 1-alkyl-3-methylimidazolium ionic liquids: a combined pfg nmr and x-ray scattering study,” *Physical Chemistry Chemical Physics* **15**, 5510–5517 (2013).
 - [34] Durba Roy, Nikhil Patel, Sean Conte, and Mark Maroncelli, “Dynamics in an idealized ionic liquid model,” *The Journal of Physical Chemistry B* **114**, 8410–8424 (2010).

- [35] Florian Dommert, Katharina Wendler, Robert Berger, Luigi Delle Site, and Christian Holm, “Force fields for studying the structure and dynamics of ionic liquids: a critical review of recent developments,” *ChemPhysChem* **13**, 1625–1637 (2012).
- [36] In-Chul Yeh and Max L Berkowitz, “Ewald summation for systems with slab geometry,” *The Journal of chemical physics* **111**, 3155–3162 (1999).
- [37] Steve Plimpton, “Fast parallel algorithms for short-range molecular dynamics,” *Journal of computational physics* **117**, 1–19 (1995).
- [38] Christopher J Fennell and J Daniel Gezelter, “Is the ewald summation still necessary? pairwise alternatives to the accepted standard for long-range electrostatics,” *The Journal of chemical physics* **124**, 234104 (2006).
- [39] WJ Van Meegen and IK Snook, “Solvation forces in simple dense fluids. ii. effect of chemical potential,” *The Journal of Chemical Physics* **74**, 1409–1411 (1981).